Journal of Structural Geology 33 (2011) 1193–1205

Contents lists available at ScienceDirect

Journal of Structural Geology

journal homepage: www.elsevier.com/locate/jsg

Analogue models of second-order faults genetically linked to a circular strike-slip system

Grégory Dufréchou [a,*], Francis Odonne [a,b,c], Giulio Viola [d,e]

[a] Université de Toulouse, UPS (OMP), GET, 14 Av. E. Belin, F-31400 Toulouse, France
[b] CNRS, GET, F-31400 Toulouse, France
[c] IRD, GET, F-31400 Toulouse, France
[d] Geological Survey of Norway, 7491 Trondheim, Norway
[e] Department of Geology and Mineral Resources Engineering, NTNU, 7491 Trondheim, Norway

ARTICLE INFO

Article history:
Received 10 May 2010
Received in revised form
10 April 2011
Accepted 24 April 2011
Available online 7 May 2011

Keywords:
Circular wrench fault
Analogue experiment
Riedel faults
Second-order faults

ABSTRACT

Sandbox experiments with sand and sand-silicone models were performed above a circular strike-slip fault to understand the influence of curvature on the development of second-order faults. Riedel R faults appear already at low displacements in the concave side of the circular plate where they always form more numerous. They are followed by R faults in the convex side and eventually by throughgoing D faults that join the R faults and that develop parallel to the underlying circular fault. The angle between the Riedel faults and the trace of the main circular fault at the surface of the models is c. 26° on the concave side and 15° on the convex side. We infer a larger obliquity of σ_1 in the concave side of the circular plate, which corresponds to a larger transpressional component than in the convex side of the main wrench fault due to the more confined volume of deforming sand. In sand experiments, most of the faults root into the underlying strike-slip fault. In sand-silicone experiments instead, the faults form close to the displacement discontinuity in case of a high displacement rate only. Uplifted areas are located all along the main fault in sand experiments. In sand-silicone experiments, they are mostly located in wedges defined by the Riedel faults and the main wrench fault and the width of these uplifted areas appear to be related to the length and activity of the Riedel faults. Our results differ significantly from those of experiments with straight strike-slip faults where strain and second-order faults are symmetrically arranged on both sides of the main fault.

1. Introduction

Strike-slip faults occur at all scales and in a variety of tectonic settings, (e.g. Anderson, 1951; Moody and Hill, 1956; Wilcox et al., 1973; Segall and Pollard, 1980; Sylvester, 1988; Viola et al., 2001; Storti et al., 2003). Analogue models of strike-slip faults and their associated second-order structures have provided useful insights into their geometric, kinematic and dynamic evolution (e.g. Riedel, 1929; Emmons, 1969; Tchalenko, 1970; Ramsay and Graham, 1970; Odonne and Vialon, 1983; Richard et al., 1989a,b, 1991; Ueta et al., 2000; Viola et al., 2004).

According to Anderson (1951), strike-slip faults develop ideally at a sub-vertical planar attitude, parallel to σ_2, the intermediate and vertical principal stress direction, in this case. With an internal friction angle of 30°, σ_1 is orientated at 30° to the fault strike (Jaeger and Cook, 1969; Byerlee, 1978). However, the upward decrease of fault dip angle commonly observed in flower structures is strong evidence for the nonpure strike-slip character of the displacement along natural wrench faults, indicating that transpressional and transtensional components are also accommodated along the fault planes (e.g. Sanderson and Marchini, 1984; Jamison, 1991; Dewey et al., 1998). Typically, experiments simulated deformation and faulting along straight strike-slip faults generated by a pure strike-slip basal displacement (Riedel, 1929; Emmons, 1969; Mandl, 1988; Richard and Cobbold, 1989, 1990; Richard et al., 1989a,b). To reproduce more complex and at times more realistic deformation, contractional or extensional behaviours were added to the strike-slip displacement component in some experimental works (e.g. Naylor et al., 1986; Keller et al., 1997; Schreurs and Colletta, 1998; McClay and Bonora, 2001; Viola et al., 2004).

Remarkable natural examples of arcuate or curved wrench faults are also known, such as the north Anatolian (e.g. Dhont et al., 1998) and the Denali faults (Glen, 2004; Redfield et al., 2007). In the case

* Corresponding author. Present address: INRS Eau Terre Environnement, 490 de la Couronne, Québec (QC) GIK 9A9, Canada. Fax: +1 418 654 2600.
E-mail address: gregory.dufrechou@ete.inrs.ca (G. Dufréchou).

0191-8141/$ – see front matter © 2011 Elsevier Ltd. All rights reserved.
doi:10.1016/j.jsg.2011.04.002

of the Ailao Shan-Red River shear zone, a curved geometry has also been proposed at the continental scale to support a model of crustal extrusion (zipper tectonics; Leloup et al., 2001; Anczkiewicz et al., 2007 and references therein). The curved geometry of these faults introduces an extra geometric element to deformation that can be usefully investigated for the analysis of large-scale strike-slip systems, partially because our current understanding and interpretation is generally based on the knowledge derived from the study of linear strike-slip fault systems (Riedel, 1929; Tchalenko, 1970). The 3D geometry and kinematics of structures associated with curved strike-slip deformation in analogue models were in part explored by Emmons (1969), whose experiments showed that most of the induced faults root down into the curved displacement discontinuity at the base of the models and that reverse faults accommodate volumetrically diffuse lateral thrusting.

To understand better the influence of the curvature on such circular wrench faults, we deformed sand and sand-silicone experiments over a moving circular plate. The aim of our study is to investigate the dynamic evolution of a circular strike-slip fault with a specific focus on the nucleation, development and kinematics of its second-order structures. Their geometric arrangement is used to infer the geodynamic process and stress-state of the upper crust during this deformation. Models with a silicone layer at the base reproduced simplistically a mechanical stratification of the crust with a ductile horizon underlying a brittle one, whereas models of sand were analogues for the brittle crust.

2. Experimental setup and materials

2.1. Experimental setup

In our analogue experiments, the circular strike-slip movement was produced by the clockwise rotation of a quarter of a circular metallic plate (Fig. 1a) with a radius of 50 cm. The plate rested on a larger metallic plate attached to a sturdy study table (110 cm × 80 cm). The rotation axis of the circular plate corresponded exactly with the geometrical centre of the plate, so that no "induced" transpressional or transtensional components were introduced during rotation. Displacement was generated and controlled by a computer-driven stepper motor that pulled the plate at a constant rate (Fig. 1a). The motor produced an angular rotation of the plate but, given the constant radius of the plate, the displacement can be expressed as a tangential velocity along the circular boundary of the plate. Displacement rates varied from 4 to 25 cm/h along the plate boundary in our experiments.

Table 1
List of experiments and principal experimental parameters.

Experiment	Materials	Displacement	Displacement rate
A	Sand (4 cm)	2 cm	about 25 cm/h
B	Sand (4 cm)	2 cm	about 25 cm/h
C	Sand (4 cm)	5 cm	about 25 cm/h
D	Sand (4 cm)	10 cm	about 25 cm/h
E	Sand (4 cm)	20 cm	about 25 cm/h
F	Sand (4 cm)	20 cm	about 25 cm/h
G	Sand (3 cm) Silicone (1 cm)	5 cm	4 cm/h
H	Sand (3 cm) Silicone (1 cm)	5 cm	25 cm/h
I	Sand (3 cm) Silicone (1 cm)	5 cm	10 cm/h
J	Sand (3 cm) Silicone (1 cm)	20 cm	10 cm/h
K	Sand (3 cm) Silicone (1 cm)	20 cm	25 cm/h

All the experiments covered a 60 cm × 60 cm square on study table (Fig. 1a) and were laterally unconfined so as to reduce boundary effects. The thickness of the models was 4 cm for all experiments. A first set of experiments was performed on models composed of dry sand only, and a second set of experiments was performed on layered silicone and sand models. White and coloured sands were sieved by hand onto the table to create a succession of visual marker horizons. Coloration of sand did not alter mechanical properties, so the coloured horizons constitute purely passive markers (Mulugeta and Koyi, 1987) that were used to track vertical offsets along fault planes deforming the sand cake. A grid with a spacing of 5 cm was created on the top surface and formed a reference frame for evaluating fault propagation and displacements on the horizontal top free surface. Photographs of the free surface were taken at regular displacement intervals. At the end of each experiment, the model was saturated in water (Richard and Krantz, 1991) to permit vertical sectioning perpendicular to the circular edge of the plate.

Experimental results are presented in top view and in section. The pictures are labelled by three letters: GD, for all pictures, and A to K plus a number. Letters GD are common for all experiments,

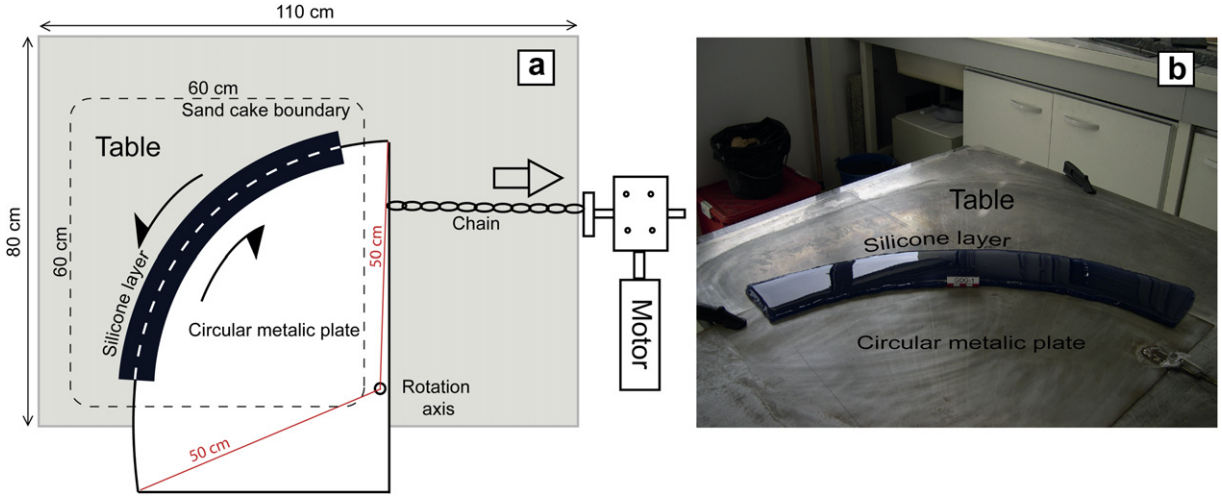

Fig. 1. a) Top view of the apparatus showing the table, the rotation direction of the circular metallic plate and the stepper motor, b) Picture of the 10 cm wide silicone layer over the edge of the circular plate.

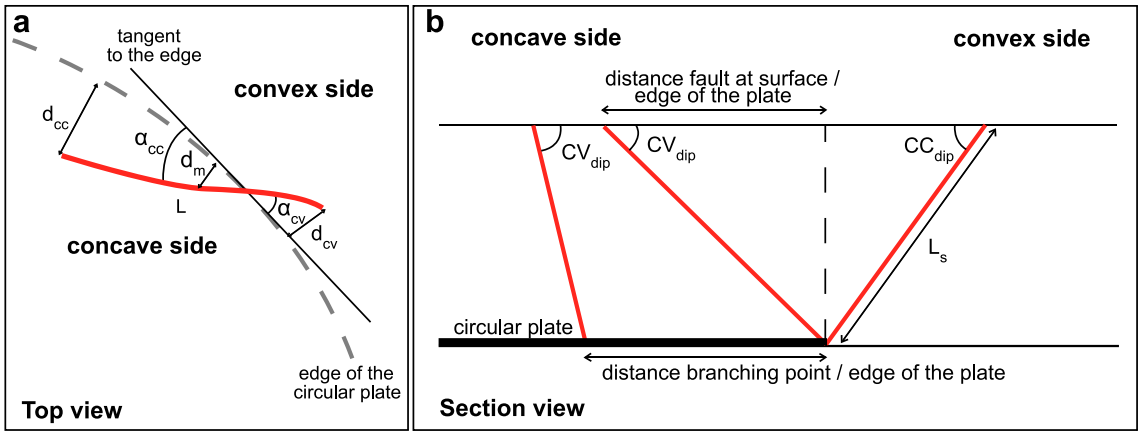

Fig. 2. Illustration of measurement geometry from top views and vertical sections in the experiments. a) Top view measurements: "L" is the fault length; "d_{cc}" is the distance between the concave side fault tip and the edge of the circular plate; "d_{cv}" is the corresponding measurement on the convex side; "d_m" is the distance between the fault mid length point and the circular plate; "α_{cc}" is the angle, above the concave side, between the fault direction and the tangent to the edge of the plate and "α_{cv}" is the corresponding measurement on the convex side. b) Section measurement: "CV_{dip}" is the fault dip facing to the convex side of the experiment; "CC_{dip}" is the fault dip facing the concave side; "L_s" is the trace of the fault length on the section.

whereas letters A to K represent different experiments. In top view, the numbers quantify the displacement of the underlying strike-slip fault. Numbers in section view are arbitrary, as they are used to name and archive each picture. To simplify the description of the results and the discussion, we only report the third letter of each set of experiments (Table 1).

Experiments A to F (Table 1) were composed exclusively of sand. Experiment A was built with horizontal sand layers with constant thickness. Unfortunately, because pure strike-slip displacement does not generate a significant vertical component, it was difficult to observe the trace of pure strike-slip faults in the vertical sections. To avoid that, in experiments B to F we sieved coloured sand into layers with variable thicknesses. In these experiments, where thick portions of layers may be juxtaposed against thinner parts of the same layers, strike-slip faults are clearly visible on the sections, even for small displacements of the circular plate. On the other hand, the variable thickness made it difficult to characterize the vertical displacement along nonpure strike-slip faults. For this reason, layers with constant thickness were prepared for the remaining experiments, G to K.

The basement fault is represented by the edge of the circular plate and forms a distinct boundary in the displacement field. In nature, the displacement field is not always so distinct and the strike-slip-generated strain may be accommodated over a larger area. To reproduce and investigate distributed deformation, we introduced the silicone layer at the base of the sand. It represented a relatively weaker and more ductile layer, providing a detachment horizon at depth. G to K experiments (Table 1) contained the 1 cm thick and 5 cm wide layer of silicone putty laid straight onto the edge of the circular plate (Fig. 1b). The sand was then sieved onto the silicone and plate, up to a complete thickness of 4 cm, as in the experiments without silicone.

2.2. Materials and scaling laws

Rocks of the upper crust are assumed to have a brittle Coulomb behaviour with a generally low cohesion and an angle of internal friction between 30° and 40° (Byerlee, 1978; Brace and Kohlstedt, 1980). Consequently, pure quartz sand is widely used in analogue experiments to represent the brittle behaviour of the upper crust (Hubbert, 1951; Mandl, 1988; McClay and White, 1995; Brun and Nalpas, 1996). In our experiments, a pure quartz sand of aeolian origin was used (Fontainebleau sand from the Paris Basin, France) with low cohesion $C \approx 500$ Pa, a density $\rho = 1.493$ g cm^{-3} (Krantz, 1991) and an angle of internal friction φ between 30° and 35° (Krantz, 1991; Dubois et al., 2002). The sand obeys the Mohr–Coulomb failure criterion and imposed strain is accommodated along discrete fault surfaces or narrow dilating deformation bands (Mandl et al., 1977; Mandl, 1988; Krantz, 1991). Its brittle behaviour is considered as time independent and, because proportionality exists between the stresses in two materials having the same angle of internal friction and low cohesions, experiments with sand scale to reproduce the brittle

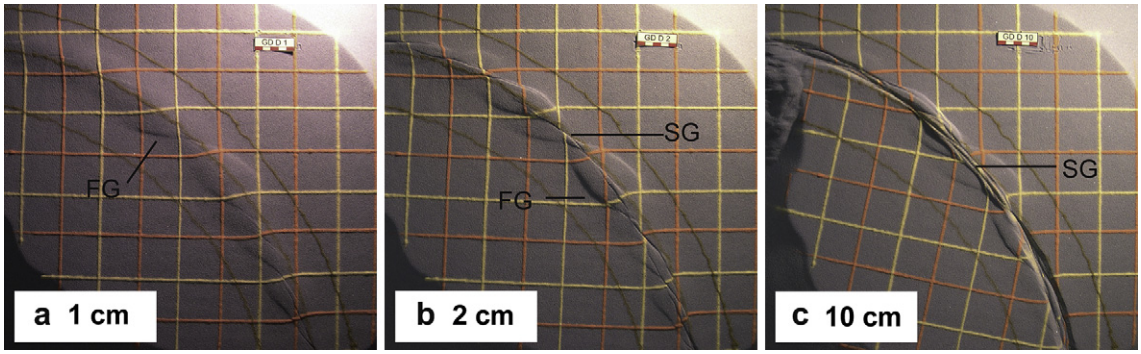

Fig. 3. Photographs of three successive stages of experiment D (pure sand), showing the fault pattern evolution during progressive deformation after 1 cm displacement (a), after 2 cm displacement (b), after 10 cm displacement (c).

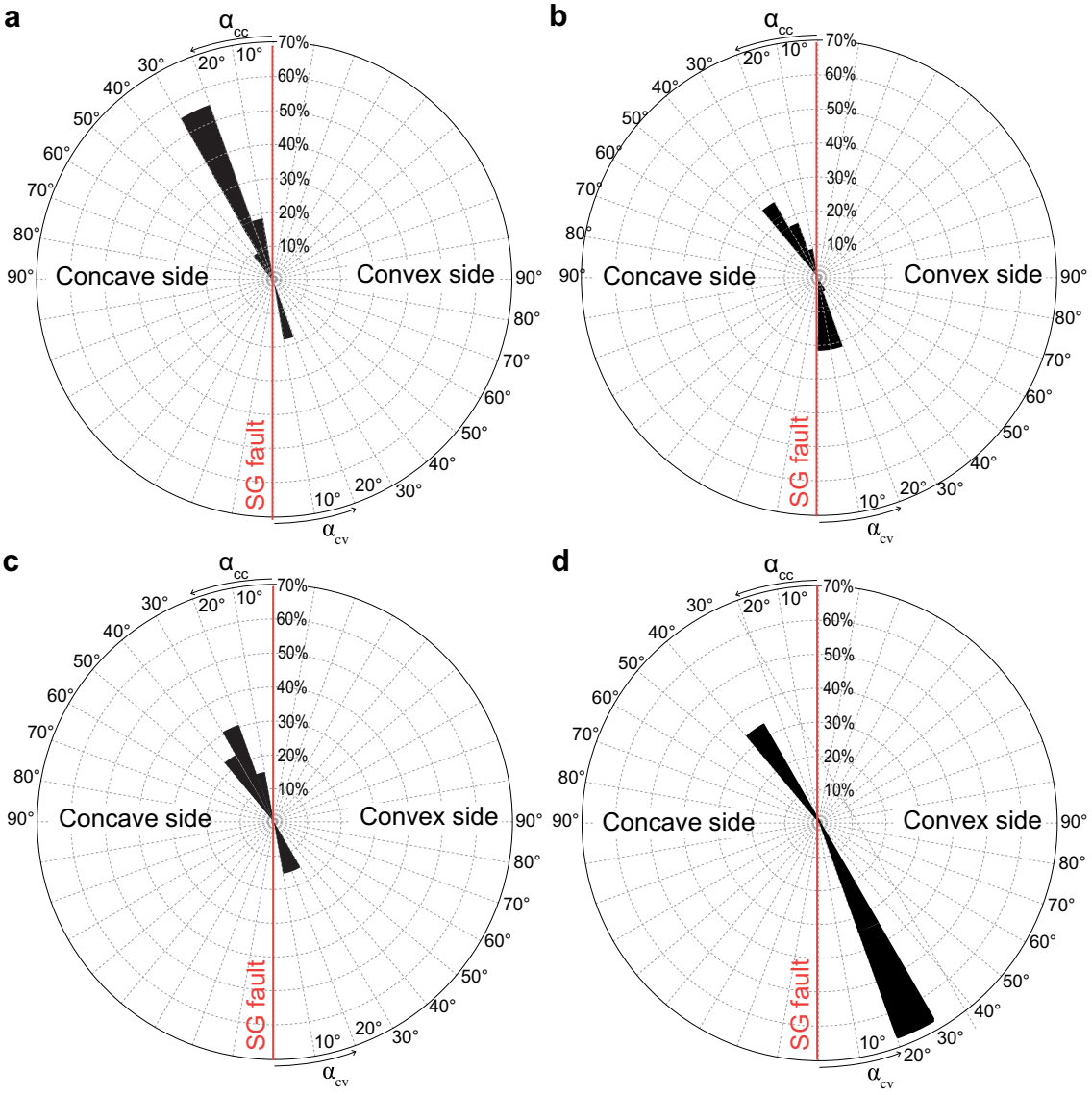

Fig. 4. Angle between FG and SG faults traces for experiments B (a), C (b), D (c) and F (d); all experiments are only with sand. The upper left quadrant of each rose diagram displays the angle α_{cc} above the concave side of the circular plate, whereas the lower right quadrant displays the angle α_{cv} above the convex side of the circular plate.

part of the upper Earth's crust (Hubbert, 1951; Horsfield, 1977; Richard et al., 1989a).

The silicone material in our experiments is PDMS (DOW CORNING SGM 36). It has a viscosity of 5×10^4 Pa (Weijermars and Schmeling, 1986) and a density $\rho = 0.965$ g cm^{-3}. The strain rate imposed on the silicone putty during our experiments varied between 1×10^{-3} s^{-1} and 7×10^{-3} s^{-1}, corresponding to the strain rate domain in which SGM 36 behaves as a Newtonian viscous fluid (Weijermars and Schmeling, 1986). Considering $\xi = \eta V/k\rho gh$, (where ξ is the characteristic screening length, V is the displacement velocity, η the ductile viscosity, k the friction coefficient, and ρgh is the lithostatic pressure at the base of the brittle layer) to determine whether gravitational or viscosity forces dominate (Sornette et al., 1993), $\eta = 5 \times 10^4$ Pa s yields screening lengths in our experiments of 2 mm, 5 mm and 1.2 cm for displacement velocities of 4, 10 and 25 cm/h respectively. Our experiments are therefore mainly controlled by gravity forces, although those with displacement rates of 25 cm/h have small-scale deformation controlled by viscosity forces. As a result, our sand-silicone experiments are scaled to represent the deformation of upper crustal rocks responding in a brittle fashion to deformation while resting over a ductile horizon, such as evaporites. At small displacement rates, the experiments are controlled by gravity forces and PDMS silicone acts as a soft decoupling horizon (Ranalli, 1995). At greater displacement rates, viscosity forces increase and the silicone layer behaves as a stronger material, acting as a glue or adhesive layer.

3. Experimental results

To better quantify the results of the experiments and define experimental parameters that can be easily compared, measurements were made on the upper surface of the models during and after deformation and on the vertical sections. Measurements are distinguished between "concave" and "convex" depending on whether they were made on structures occurring within the concave or convex side of the circular plate, respectively. Parameters measured on the top free surface (Fig. 2a) are:

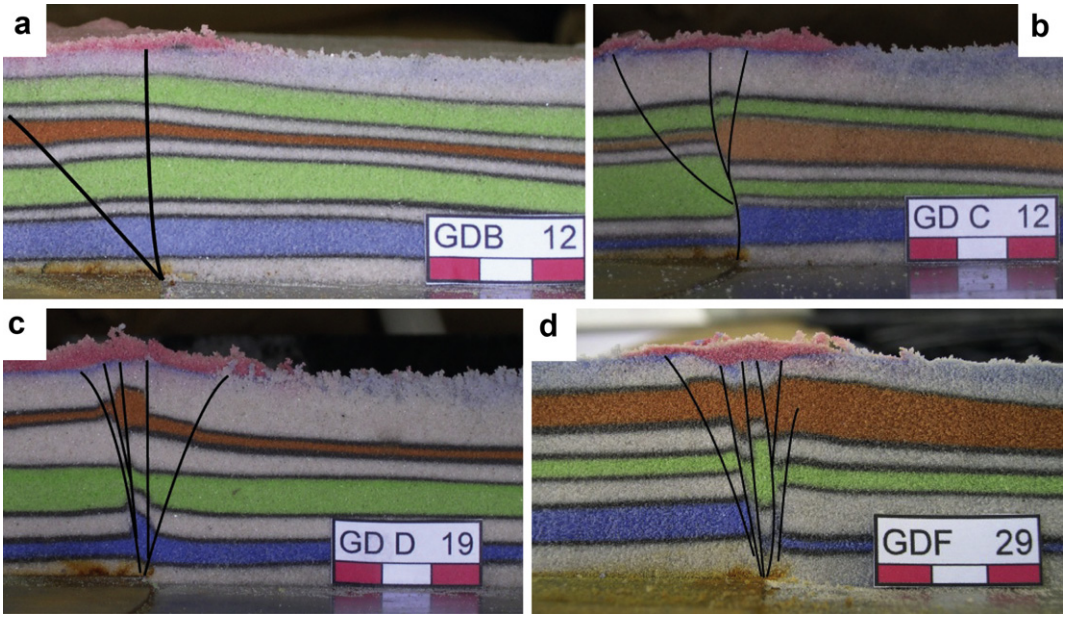

Fig. 5. Photographs of selected examples of vertical sections from experiments B, C, D and F. a) Experiment B (final displacement 2 cm); b) experiment C (final displacement 5 cm); c) experiment D (final displacement 10 cm); d) experiment F (final displacement 20 cm).

- "L", the fault length;
- "d_{cc}" and "d_{cv}", the distance between fault tips and the edge of the circular plate measured perpendicular to the fault (i.e. parallel to the radius of the circular fault), for the concave and convex side of the fault tip, respectively;
- "d_m", the distance between the mid-point of the fault, that is the point taken at the half-length of the fault, and the edge of the circular plate;
- "α_{cc}" and "α_{cv}", the angles formed by the intersection between the fault trace and the tangent to the edge of the mobile circular plate, above the concave and the convex sides of the model, respectively.

Sections were cut along radial directions such that they always ran perpendicularly the edge of the circular plate. In all figures, the concave part of the sections is always on the left side. Parameters measured from the sections (Fig. 2b) are:

- "CV_{dip}", the fault dip, which is a "convex dip" when the fault plane faces the convex side of the model;

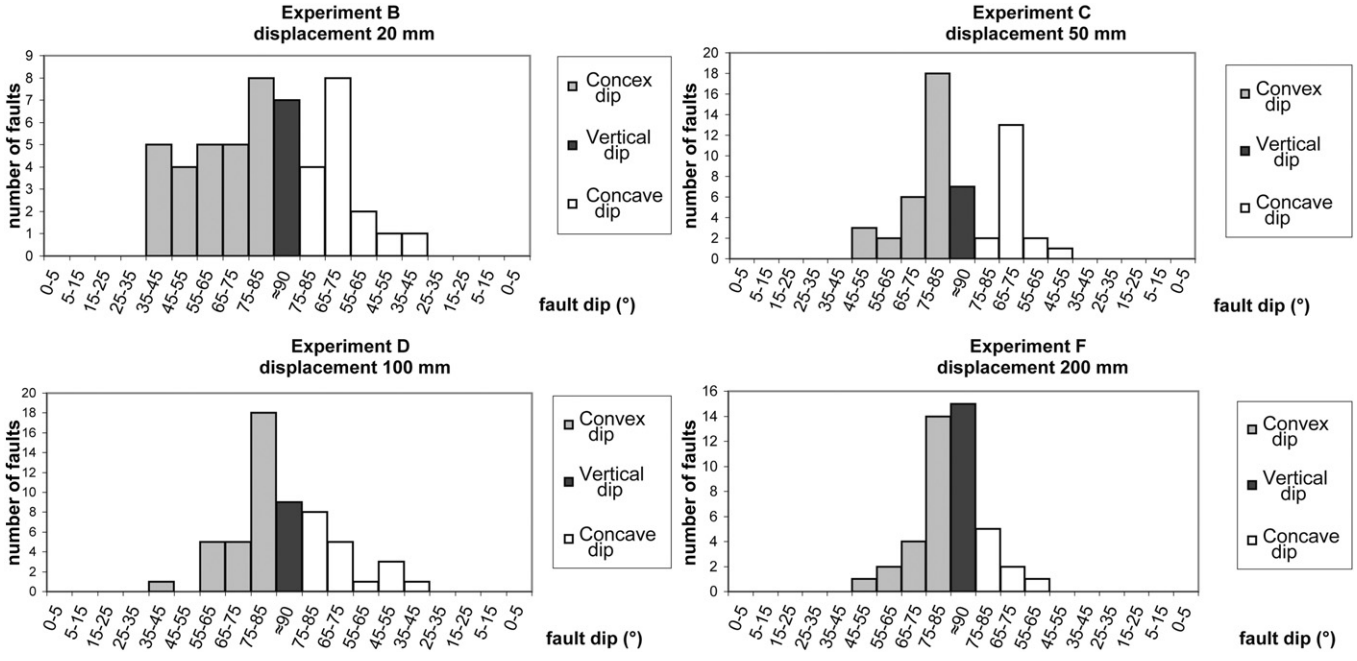

Fig. 6. Dip values for experiments B, C, D and F. Convex dips and concave dips are plotted separately.

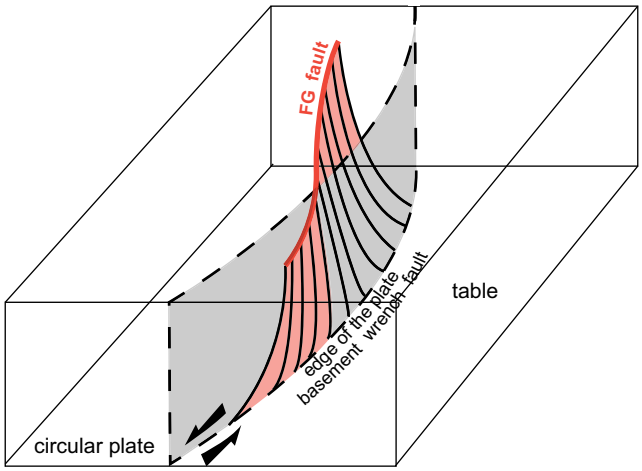

Fig. 7. Schematic 3D figure illustrating the geometry of a first generation (FG) fault.

- "CC_{dip}", "concave dip" when the fault dips towards the concave side of the model;
- "L_s", the fault length measured on the section.

In addition, we measured systematically the distance between the fault at the surface of the experiment and the edge of the circular plate and the distance between the branching point of the fault at depth and the edge of the circular plate.

3.1. Results of sand experiments

A total of 6 experiments were run with only sand (Table 1). Results were found to be comparable throughout the series. Therefore, we illustrate the main results with representative photographs from only four experiments.

Progressive fault growth is shown by the successive top views of the sand cake. The first faults to appear are in here referred to as "first generation" faults (FG). They are arranged in an "en echelon" fashion and follow the curved geometry of the basement circular fault. They nucleate systematically at very early stages of deformation, and are clearly visible already after only 1 cm of tangential displacement (Fig. 3a). They form predominantly in the concave part of the master basement fault. After their nucleation, they propagate and extend to both sides of the edge of the circular underlying fault, although they always remain better developed in the concave part. After displacements larger than 2 cm (Fig. 3b), the FG faults become interconnected by throughgoing second-generation faults (SG) that form mainly above the edge of the plate. During subsequent deformation, the FG faults become inactive. By the end of the experiments for displacements of 10 cm (Fig. 3c), only the later faults, roughly parallel to the edge of the plate, are still active.

The angle measured on the model surface between the direction of the FG faults and the tangent to the circular plate differs depending on whether the fault is within the concave or convex side of the plate (see summary diagram for experiments B in Fig. 4a, C in Fig. 4b, D in Fig. 4c and F in Fig. 4d). On the concave side of the plate the mean value of α_{cc} is 26°, whereas α_{cv} is 15° on the convex side.

Fault dips are measured easily in the sections. Our observations show that for small displacement values (2 cm; Table 1), dip angles range from 40 to 90°, with a prevalence for smaller dips (experiment B in Fig. 5a). For greater displacement (e.g. 5 cm–20 cm; Table 1), the number of steep and vertical faults increases (e.g. experiments C in Fig. 5b, D in Fig. 5c and F in Fig. 5d). Because most faults root down into the edge of the circular plate and because FG faults grow to greater distances from this plate boundary, the latter have low dip values. This is consistent with the observations made for the experiments with low values of finite displacement. For larger displacements, numerous SG faults are present and root down steeply into the circular plate boundary. In addition, as shown in Fig. 6, most of the faults are located on the concave side of the plate boundary. The geometry of FG faults, as reconstructed from horizontal serial sections, is helicoidal (see the 3D fault diagram of Fig. 7), in agreement with the observations of Naylor et al. (1986) and Ueta et al. (2000).

3.2. Results of experiments with sand and silicone

For the low-velocity experiment (Experiment G; Fig. 8), faults formed almost exclusively in the concave part of the sand cake. FG faults formed first and, after a displacement of 2 cm, they were progressively connected and cut through by SG faults. At the end of the deformation process, SG faults linked up to form a single active throughgoing fault parallel to the edge of the circular plate, but located about 3 cm inside of it, that is, within the concave side of the model (Fig. 8a). Vertical sections show that the faults root down at depth between the edge of the circular plate and the boundary of the silicone layer but have different positions relative to the underlying circular plate as a function of displacement rates (Fig. 8b). Most faults have large dip values and many face to the convex side of the model.

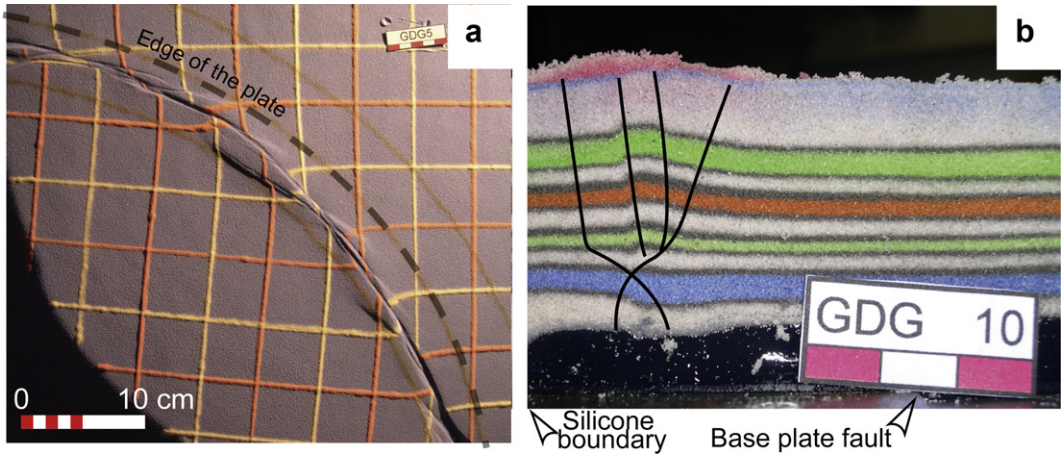

Fig. 8. Top view (a) and vertical section (b) of experiment G.

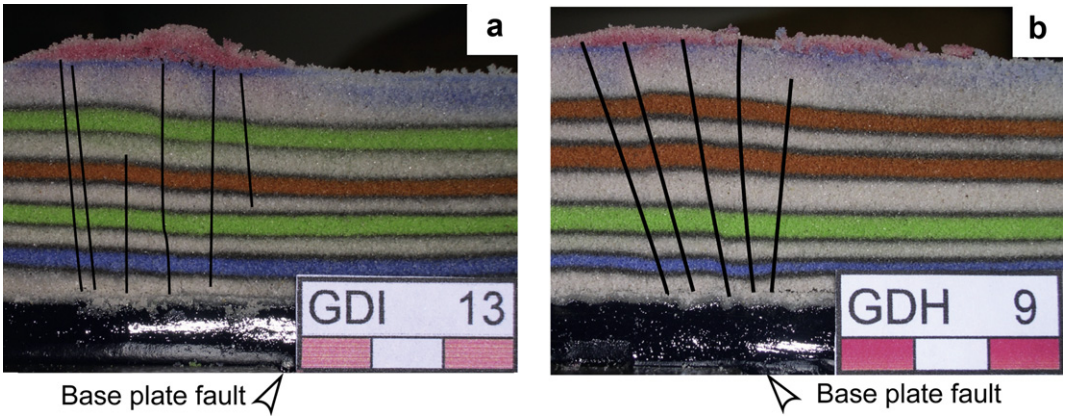

Fig. 9. Vertical sections from experiments I (a) and H (b), both sand-silicone experiments with a 5 cm total displacement.

For the medium to high velocity experiments (experiment I in Fig. 9a and H in Fig. 9b), the same fault evolution was observed with the formation of early FG faults, and then connection by SG faults. Consideration of experiments G, I and H (Figs. 8 and 9), shows that the sub-vertical faults in the sand root to a position at the top of the silicone layer that is closer to the underlying circular plate edge with increasing displacement rate. Thus, whereas in experiment I with a displacement rate of 10 cm/h, faults are located 2 cm from the edge of the plate (Fig. 9a), they are almost above it in experiment H, deformed at a faster 25 cm/h displacement rate (Fig. 9b).

In experiments G, I and H (Figs. 8 and 9) where final displacement is 5 cm, the number of faults with a convex dip was always larger than the number with a concave dip, irrespective of displacement rate (Table 2).

As in the sand experiments, the angle at the surface between the FG faults and the tangent to the circular plate differs between the concave or convex side of the deforming domain. On the concave side of the plate, α_{cc} varies between 20° and 26° whereas α_{cv} is between 13° and 15° on the convex side (Table 2). These values are a few degrees less than in the experiments with sand only, but α_{cc} is always greater than α_{cv} (Fig. 10).

3.3. Uplifted and depressed areas in the experiments

The uplifted blocks recognized in our experiments were used to identify volumes affected by local transpression, whereas topographically depressed volumes were taken to indicate local transtensional conditions (e.g. Dewey et al., 1998; Schreurs and Colletta, 1998). Each experiment was sectioned from 25 to 32 times, with c. 2 cm spacing. From these serial sections and the recording of the uplifted and depressed blocks on the top view of the models, it was possible to build maps of the topographically uplifted and depressed areas associated with circular wrench faults.

For sand experiments C and D, the uplifted and depressed areas are located in a narrow strip above the edge of the circular plate (Fig. 11). In experiment C, short and narrow uplifted and depressed areas form isolated and lensoidal domains along this boundary (Fig. 11a). However, for greater displacements in experiment D, these areas are longer and broader, following one another along the edge of the plate (Fig. 11b).

In sand-silicone experiments G and H, only the displacement rate differed, being 4 cm/h in G and 25 cm/h in H. In experiment G, although distributed more or less continuously along the throughgoing SG fault, uplifted areas are confined to isolated structural domains bound by FG and SG faults and, in addition, only a few depressed areas are present (Fig. 12a). For the fast strain-rate experiment H, uplifted areas occur almost continuous above the edge of the circular plate while depressed areas are very limited in occurrence (Fig. 12b). The uplifted domains are mostly located between contiguous pairs of FG faults and many more are developed than in sand and sand-silicone experiments at the slower displacement rate.

The analysis of the sections from these experiments shows that the faults are conjugate and form hourglass structures (Gartrell et al., 2006). Conjugate faults merge to a common point in the lower or medium part of the sand cake and define two wedges that diverge in the case of uplift (as indicated by the white arrows of Fig. 13a) and that instead converge in the case of a depression (Fig. 13b). Uplifted and depressed areas can be interpreted as an isostatic response of the silicone layer to the vertical juxtaposition of small sand wedges passively carried along the circular strike-slip

Table 2
Principal features of experiments G, I and H that all have a 5 cm complete displacement.

Experiment	Displacement rate	Nb. of convex dip faults	Nb. of concave dip faults	R faults α_{cc}	R faults α_{cv}
G	4 cm/h	31	10	21.75	14.75
I	10 cm/h	33	19	19.7	13.0
H	25 cm/h	49	14	26.0	14.43

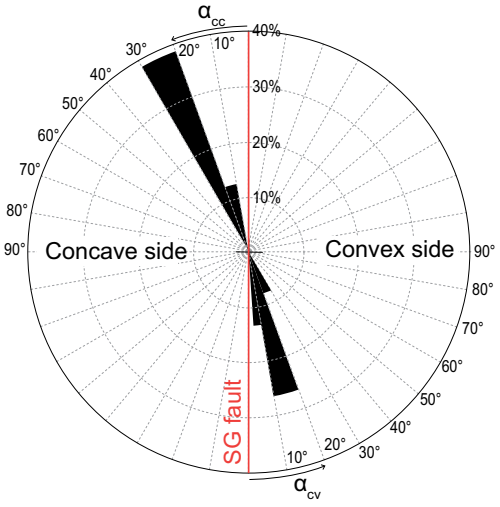

Fig. 10. Angle between FG and SG faults traces for experiments G, H and I; all experiments are with sand and silicone. The upper left quadrant of each rose diagram displays the angle α_{cc} above the concave side of the circular plate, whereas the lower right quadrant displays the angle α_{cv} above the convex side of the circular plate.

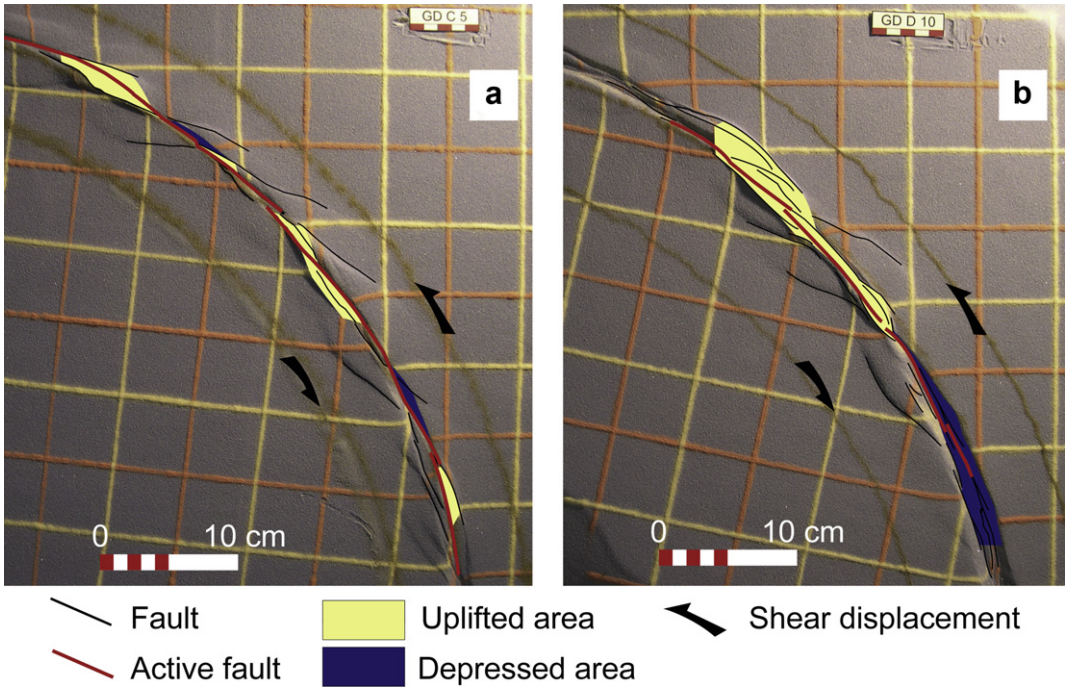

Fig. 11. Location of topographically depressed (transtensional) and uplifted (transpressional) areas on sand models for experiments C (a) and experiment D (b). Active faults are located above the edge of the circular plate.

fault. Under uplifted areas the silicone layer is thinner while it is thicker under depressed regions (Fig. 13).

4. Synthesis and discussion

4.1. Models characteristics and singularities

In both sets of experiments, FG faults always form at the early stages of displacement, and they can be interpreted as synthetic Riedel shears (R shears; Riedel, 1929; Tchalenko, 1968; Bartlett et al., 1981). They are followed by SG faults that connect the R faults and are interpreted as D faults (Tchalenko, 1968, 1970; Boudon et al., 1976). The main difference between sand and sand-silicone models is that R faults appeared for less displacement (1 cm) in the sand models than in the sand-silicone models (2 cm). In the latter, the sand cake begins to accommodate strain in a more volumetrically diffuse fashion before the first discrete faults appear and strain localizes.

In the experiments with only sand, most faults root into the edge of the circular plate. As a result, the more distant faults are from the edge of the circular plate, the lesser their dips. This change is particularly clear for experiments B (Fig. 14a) and D (Fig. 14b). On the other hand, in our experiments with sand and silicone, faults do not root right into the edge of the circular plate. Second-order faults are located above the concave part of the circular plate for

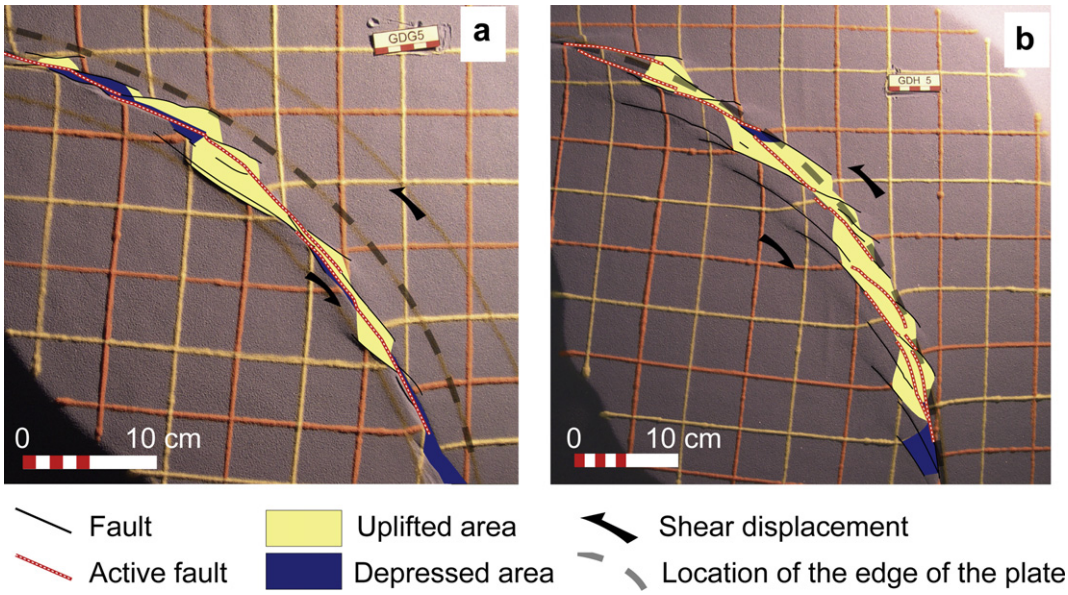

Fig. 12. Location of topographically depressed and uplifted areas for two sand-silicone experiments: experiment G (a) with 4 cm/h displacement rate and experiment H (b) with 25 cm/h.

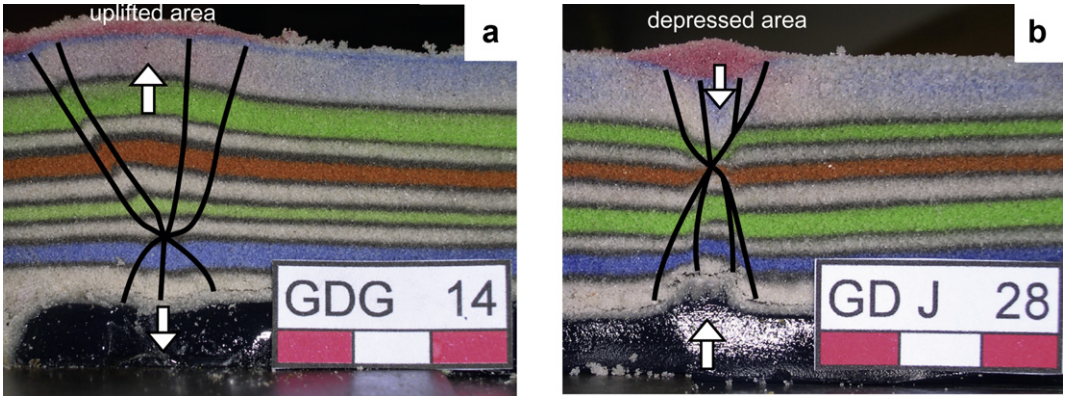

Fig. 13. Vertical sections in sand-silicone experiments G (a) and J (b) with line drawings to show fault geometries and the block relative movements.

a displacement rate of 4 cm/h (experiment G; Fig. 15a), whereas they are closer to the plate edge for greater displacement rates (experiment H; Figs. 9b and 15b). In these experiments, most faults are located on the same side of the circular plate, although a relationship between the dip and the position of the fault is not obvious.

The prevalence of topographically uplifted blocks over depressed volumes is common in our experiments. It is likely due to the fact that granular materials obey the Mohr–Coulomb failure criterion and that faults are essentially dilatant shear zones (Mandl, 1988; Krantz, 1991). In sand experiments, uplifted areas are concentrated along a narrow strip above the edge of the circular plate. In sand and silicone experiments, they are generally larger and occur mostly in fault-bound wedges between R faults and in places cross the throughgoing D fault trace, parallel to the underlying strike-slip fault. Locally, segments of the main D fault also form a boundary to the uplifted wedges. This geometric pattern may be related to the distribution of the relief around fault tips (Chinnery, 1961). At early stages of the deformation process, uplifted areas form in the compressed domains around the tips of contiguous R faults (Fig. 16). Active R faults are then progressively replaced by D faults and the interaction of the opposite displacements along D and R faults can cause further and localised vertical uplift in narrow corridors and wedges along the main wrench fault and enhance positive relief development.

4.2. Comparison between curved and straight strike-slip faults

Richard et al. (1989a) performed a series of classic physical models for straight strike-slip faults scaled to represent the brittle behaviour of the upper crust and ductile behaviour of evaporites (Figs. 17a, b and 18a, b). Our models for curved strike-slip faults retain many of the features observed in their experiments, such as the first-order geometry of R faults, their geometric and kinematic development

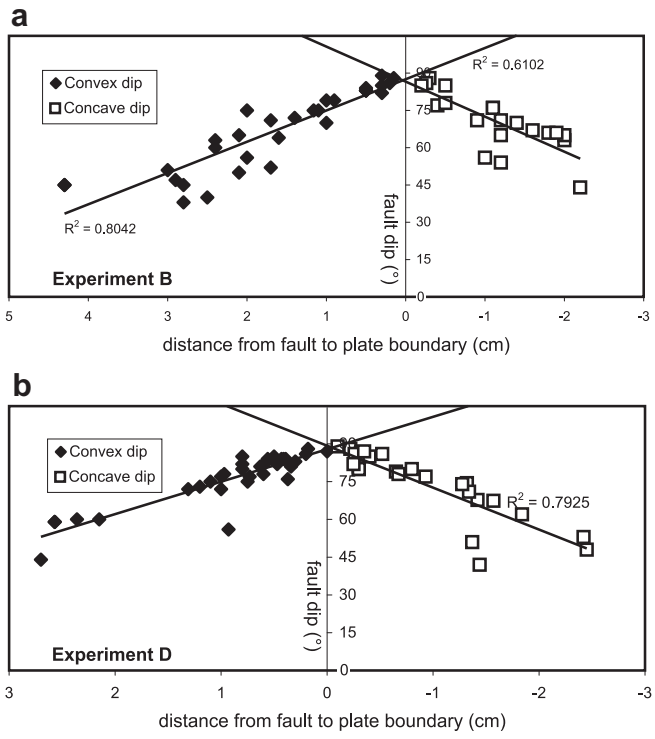

Fig. 14. Distance from faults to plate edge vs. fault dip. Total displacement for experiment B is 2 cm (a), 10 cm for experiment D (b).

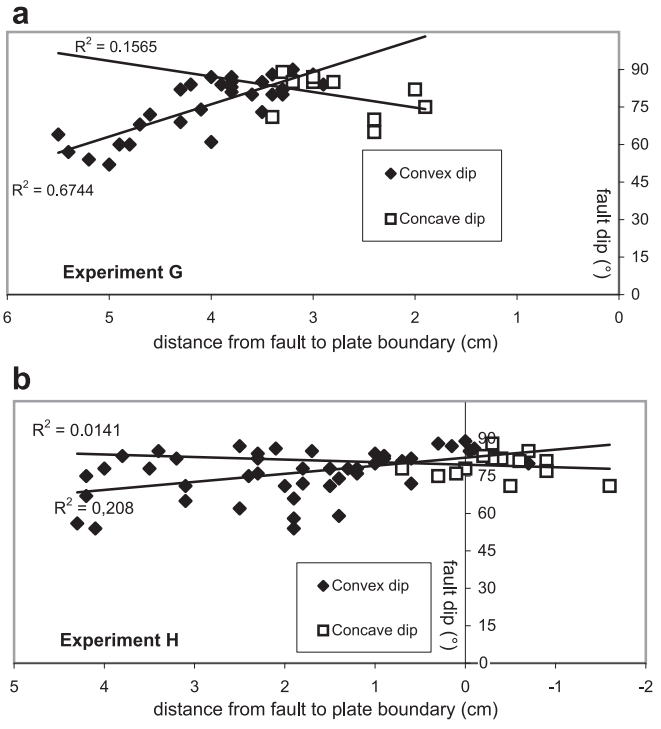

Fig. 15. Distance from faults to plate edge vs. fault dip. Total displacement is 5 cm in both experiments but displacement rate is 4 cm/h for experiment G (a) and 25 cm/h for experiment H (b).

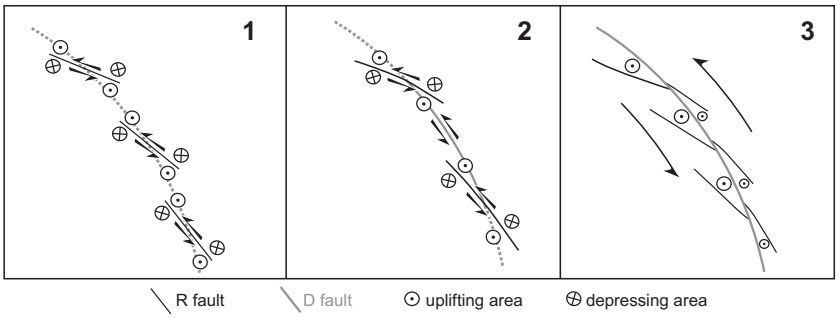

Fig. 16. Line drawing showing the propagation of faults and the distribution of depressed and uplifted areas: 1) formation of R faults on the concave side of the circular plate; 2) propagation of R faults and formation of D faults that join contiguous pairs of R faults; 3) uplifted areas resulting from opposing movements along R and D faults.

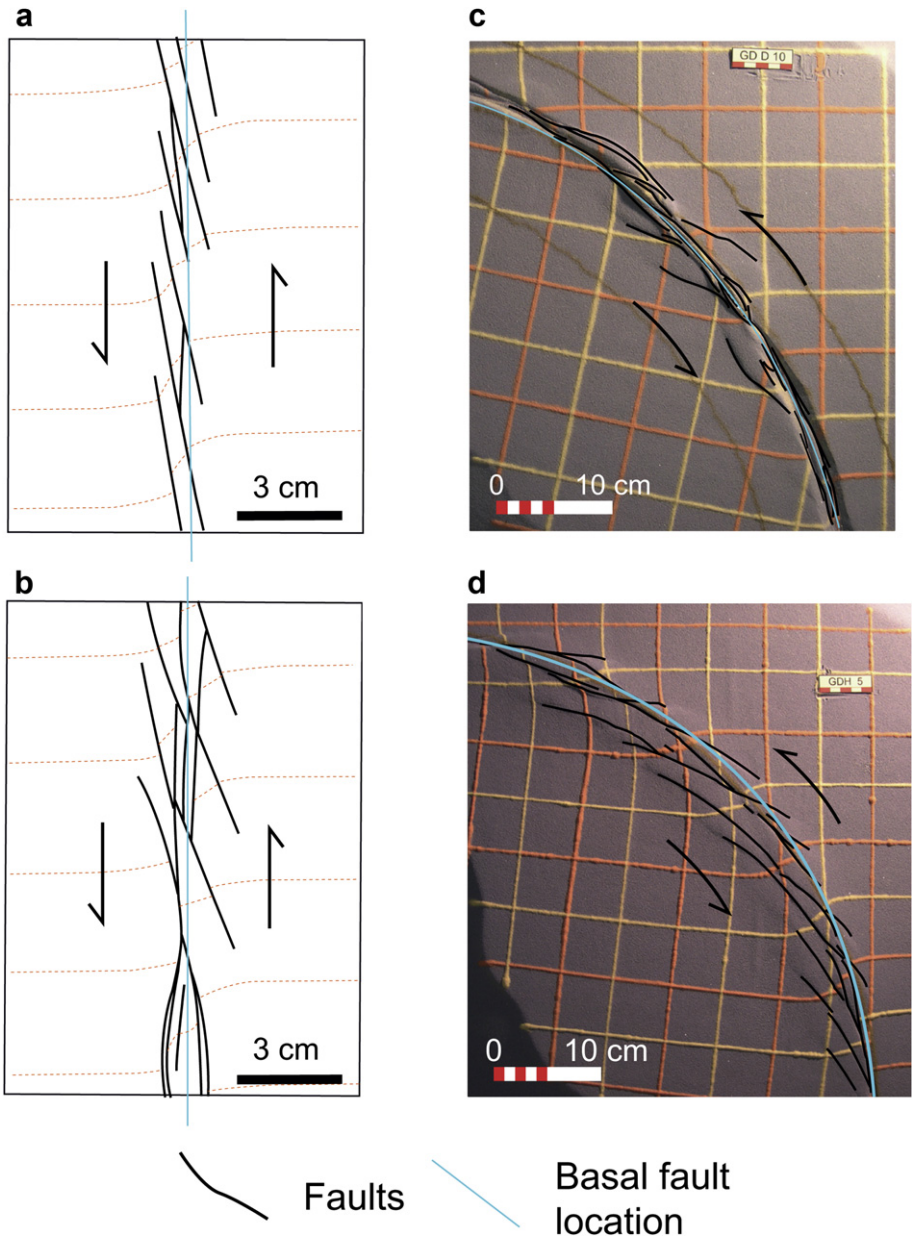

Fig. 17. Top view of pure strike-slip fault experiments of Richard et al. (1989a) respectively with sand/pyrex (a) and with sand/pyrex/silicone (b), and of circular strike-slip fault experiments with sand (c) and sand/silicone (d).

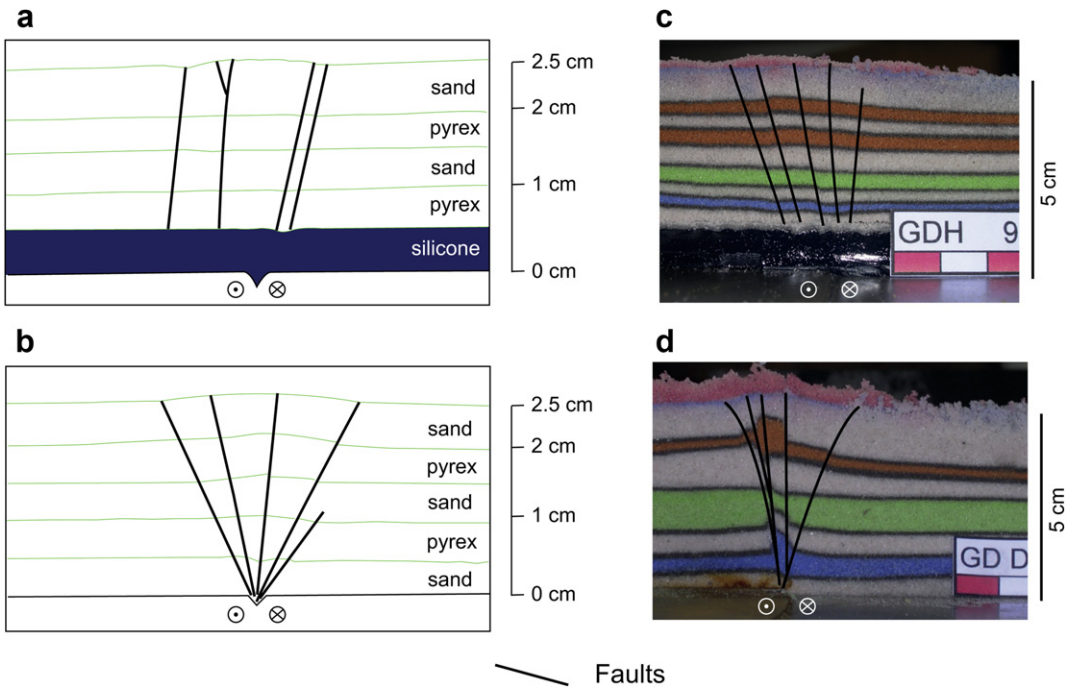

Fig. 18. a and b, Schematic line drawing of faults in straight strike-slip fault experiments of Richard et al. (1989a) with sand/pyrex and with sand/pyrex/silicone. c and d, faults a seen in vertical sections of our circular strike-slip fault experiments, with sand and sand/silicone, respectively.

and hierarchical nucleation and growth (Riedel, 1929; Tchalenko, 1970; Mandl, 1988; Sylvester, 1988; Richard and Cobbold, 1989).

The careful comparison of our experiments with those models, however, also highlights some clear differences mostly with respect to geometry and location of faults (Figs. 17c, d and 18c, d). Physical models of strike-slip faulting associated with a basement fault of constant strike (e.g. Mandl, 1988; Richard and Cobbold, 1989, 1990; Richard et al., 1989a), show that the angle between R and D is constant for both sides of the underlying straight strike-slip fault (Fig. 17a and b). The angle between throughgoing D and R faults in our experiments differs instead for the concave and convex sides of the deformed region (Fig. 17c and d) and it is consistently greater for the concave side ($\alpha_{cc} > \alpha_{cv}$; Fig. 19). The asymmetry of our experiments is readily interpreted as due to the circular shape of the basement fault.

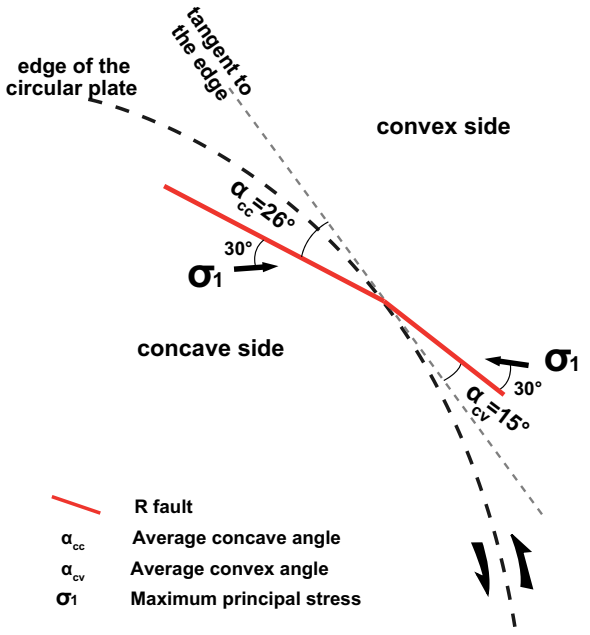

Fig. 19. Synthetic diagram showing the orientation of the principal stress σ_1 relative to the R fault trends.

As with competent rock (Jaeger and Cook, 1969; Byerlee, 1978), sand follows the Mohr–Coulomb criterion for failure with a coefficient of friction close to 0.60 (Hubbert, 1951; Krantz, 1991). Fault surfaces are therefore interpreted to be at about 30° to the direction of the maximum principal stress (σ_1). In our models, using the trend of the R faults, the direction of σ_1 can be plotted on schematic line drawings for the experiments (Fig. 19). Because $\alpha_{cc} > \alpha_{cv}$ (Fig. 19), the angle between the direction of σ_1 and the tangent to the circular D fault trace is larger on the concave side as compared to the convex side, and the transpressional behaviour could be more significant on the concave side of the deforming region. α_{cc} and α_{cv} values observed in sand and silicone experiments are only slightly smaller than in sand experiments (Figs. 4 and 10). This difference may result from a lesser friction in the throughgoing D faults. This situation can be compared to the oblique position of σ_1 due to basal friction reported in the case of a Coulomb wedge (Dahlen, 1984). Reduction in the basal friction in the wedge would reduce the obliquity of σ_1 (Hafner, 1951; Dahlen, 1984).

In the sand and pyrex model of Richard et al. (1989a), the length of R faults on the top free surface above both sides of the underlying strike-slip fault is similar (Fig. 17a and b) and faults in section are equally abundant within both blocks separated by the underlying strike-slip fault (Fig. 18a and b). However, in our experiments R faults are longer and more numerous in the concave side (Figs. 17c, d and 18c, d). Faults formed in sand experiments are dilatants shear zones (Mandl, 1988) that form when an energy threshold has been overcome by the system. The circular shape of the plate creates an asymmetry in the area for an equal width of sand on both sides of it. The area and hence, the volume is smaller above the concave side as compared to the convex side of the underlying strike-slip fault. As

a result, fault nucleation energy is dissipated in a smaller volume in the concave side, causing the failure threshold to be reached more rapidly and failure to occur earlier than in the concave side. Consequently R faults are longer (Fig. 19) and form earlier in the concave side and R and D faults are preferentially formed in the concave side of the underlying strike-slip fault (Fig. 18c and d).

5. Conclusion

Analogue experiments of a circular wrench fault have shown the successive nucleation and growth of faults in sand experiments and in sand-silicone experiments. Riedel R faults always form first in the inner side of the circular plate, and are then followed by D faults that join the R faults to form a large continuous fault zone parallel to the edge of the circular fault. The faults propagate on both sides of this boundary although they remain preferentially more numerous on the concave side.

The angle between the R faults and the main circular D fault is always more opened in the concave side of the plate (mean value 26°) than in the convex side (mean value 15°). The obliquity of σ_1 is larger on the concave side of the circular plate than on the convex side; this explains the orientation of the R faults and implies a larger transpressional component in the concave part of the main curved strike-slip fault, in turn due to a more confined volume on this side.

The succession of uplifted and depressed areas along the main fault causes significant localized relief. The uplifted areas are located all along the main fault in sand experiments. In sand-silicone experiments, uplifted areas are mostly located in wedges defined by the R Riedel faults and the main wrench fault and the width of these uplifted areas appear to be related to the length of the Riedel faults.

Circular wrench faults display the same overall geometric and kinematic evolution of second-order structures as documented for straight wrench faults. However, differences in the asymmetry of the orientation of the Riedel faults, in the location of faults, and in the repartition of the fault dips can represent relevant indications of a circular component along a wrench fault.

Acknowledgements

This paper has largely benefited of the constructive criticisms of Peter Cobbold, Lyal Harris, Fabrizio Storti, an anonymous reviewer and the editor William Dunne. Authors also thank C. Cavaré-Hester for substantial help in the line drawing of the figures.

References

Anczkiewicz, R., Viola, G., Müntener, O., Thirlwall, M., Villa, I.M., Quong, N.Q., 2007. Structure and shearing conditions in the Day Nui Con Voi massif, northern Vietnam: implications for the evolution of the Red River fault. Tectonics 6, TC2002. doi:10.1029/2006TC001972.

Anderson, E.M., 1951. The Dynamics of Faulting. Oliver and Boyd, Edinburgh.

Bartlett, W.L., Friedman, M., Logan, J.M., 1981. Experimental folding and faulting of rocks under confining pressure part IX. Wrench faults in limestone layers. Tectonophysics 79, 255–277.

Boudon, J., Gamond, J.F., Gratier, J.P., Robert, J.P., Depardon, J.P., Gay, M., Ruhland, M., Vialon, P., 1976. L'arc alpin occidental: Réorientation de structures primitivement E-W par glissement et étirement dans un système de compression global N-S. Eclogae Geologicae Helvetiae 69, 509–519.

Brace, W.F., Kohlstedt, D.L., 1980. Limits on lithospheric stress imposed by laboratory experiments. Journal of Geophysical Research 85, 6248–6252.

Brun, J.P., Nalpas, T., 1996. Graben inversion in nature and experiments. Tectonics 15, 677–687.

Byerlee, J., 1978. Friction of rocks. Pure and Applied Geophysics 116, 615–626.

Chinnery, M.A., 1961. The deformation of the ground around surface fault. Bulletin of the Seismological Society of America 51, 355–372.

Dahlen, F.A., 1984. Noncohesive critical coulomb wedges: an exact solution. Journal of Geophysical Research 89, 125–133.

Dewey, J.F., Holdsworth, R.E., Strachan, R.A., 1998. Transpression and transtension zones. In: Holdsworth, R.E., Strachan, R.A., Dewey, J.F. (Eds.), Continental Transpressional and Transtensional Tectonics. Geological Society of London Special Publication, vol. 135, pp. 1–14.

Dhont, D., Chorowicz, J., Yürür, T., Köse, O., 1998. Polyphased block tectonics along the North Anatolian fault in the Tosya basin area (Turkey). Tectonophysics 299, 213–227.

Dubois, A., Odonne, F., Massonnat, G., Lebourg, T., Fabre, R., 2002. Analogue modelling of fault reactivation: tectonic inversion and oblique remobilisation of grabens. Journal of Structural Geology 24, 1741–1752.

Emmons, R.C., 1969. Strike-slip rupture patterns in sand models. Tectonophysics 7, 71–87.

Gartrell, A., Bailey, W.R., Brincat, M., 2006. A new model for assessing trap integrity and oil preservation risks associated with postrift fault reactivation in the Timor Sea. American Association of Petroleum Geologists Bulletin 90, 1921–1944.

Glen, J.M.G., 2004. A kinematic model for the southern Alaska orocline based on regional fault patters. In: Sussman, A.J., Weil, A.B. (Eds.), Orogenic Curvature: Integrating Paleomagnetic and Structural Analyses. Geological Society of America Special Paper, vol. 383, pp. 161–172.

Hafner, W., 1951. Stress distributions and faulting. Geological Society of America Bulletin 62, 373–398.

Horsfield, W.T., 1977. An experimental approach to basement-control faulting. Geologie in Mijnbouw 56, 363–370.

Hubbert, M.K., 1951. Mechanical basis for certain familiar geologic structures. Geological Society of America Bulletin 62, 355–372.

Jaeger, J.C., Cook, N.G.W., 1969. Fundamentals of Rocks Mechanics. Methuen, London.

Jamison, W.R., 1991. Kinematics of compressional fold development in convergent wrench terranes. Tectonophysics 190, 209–232.

Keller, J.V.A., Hall, S.H., McClay, K.R., 1997. Shear fracture pattern and microstructural evolution in transpressional fault zones from field and laboratory studies. Journal of Structural Geology 19, 1173–1187.

Krantz, R.W., 1991. Measurements of friction coefficients and cohesion for faulting and fault reactivation in laboratory models using sand and sand mixtures. Tectonophysics 188, 203–207.

Leloup, P.H., Arnaud, N., Lacassin, R., Kienast, J.R., Harrison, T.M., Phan Trong, T.T., Replumaz, A., Tapponnier, P., 2001. New constraints on the structure, thermochronology, and timing of the Ailo Shan-Red River shear zone, SE Asia. Journal of Geophysical Research 106, 6683–6732.

Mandl, G., De Jong, L.N.J., Maltha, A., 1977. Shear zones in granular materials. Rock Mechanic 9, 95–144.

Mandl, G., 1988. Mechanics of Tectonic Faulting: Models and Basic Concepts. Elsevier, New York.

McClay, K.R., White, M.J., 1995. Analogue modelling of orthogonal and oblique rifting. Marine and Petroleum Geology 12, 137–151.

McClay, K., Bonora, M., 2001. Analog models of restraining stepovers in strike-slip fault systems. American Association of Petroleum Geologists Bulletin 85, 233–260.

Moody, J.D., Hill, M.J., 1956. Wrench fault tectonics. Geological Society of America Bulletin 63, 561–594.

Mulugeta, G., Koyi, H., 1987. Three-dimensional geometry and kinematics of experimental piggyback thrusting. Geology 15, 1052–1056.

Naylor, M.A., Mandl, G., Sijpesteijn, C.H.K., 1986. Fault geometries in basement-induced wrench faulting under different initial stress states. Journal of Structural Geology 8, 737–752.

Odonne, F., Vialon, P., 1983. Analogue models of folds above a wrench fault. Tectonophysics 99, 31–46.

Ramsay, J.G., Graham, R.H., 1970. Strain variation in shear belts. Canadian Journal of Earth Sciences 7, 786–813.

Ranalli, G., 1995. Rheology of the Earth, second ed. Chapman & Hall. 413 p.

Redfield, T.F., Scholl, D.W., Fitzgerald, P.G., Beck, M.E., 2007. Escape tectonics and the extrusion of Alaska: past, present, and future. Geology 35, 1039–1042.

Richard, P., Cobbold, P.R., 1989. Structures en fleur positives et décrochements crustaux: modélisation analogique et interprétation mécanique. Comptes Rendus de l'Académie des Sciences 308, 553–560.

Richard, P., Ballard, J.F., Colletta, B., Cobbold, P.R., 1989a. Naissance et evolution de failles au-dessus d'un décrochement de socle: modélisation analogique et tomographique. Comptes Rendus de l'Académie des Sciences 309, 2111–2118.

Richard, P., Loyo, B., Cobbold, P.R., 1989b. Formation simultanée de failles et de plis au dessus d'un décrochement de socle: modélisation expérimentale. Comptes Rendus de l'Académie des Sciences 309, 1061–1066.

Richard, P., Cobbold, P.R., 1990. Experimental insights into partitioning of fault motions in continental convergent wrench zones. In: Annales Tectonicae, IV, pp. 35–44 (Special Issue).

Richard, P., Krantz, R.W., 1991. Experiments on fault reactivation in strike-slip mode. Tectonophysics 188, 117–131.

Richard, P., Mocquet, B., Cobbold, P.R., 1991. Experiments on simultaneous faulting and folding above a basement wrench fault. Tectonophysics 188, 133–141.

Riedel, W., 1929. Zur Mechanik geologischer Brucherscheinungen. Ein Beitrag zum Problem der "Fiederspalten". Centralblatt für Mineralogie, Geologie und Paleontologie Abb. B, 354–368.

Sanderson, D.J., Marchini, W.R.D., 1984. Transpression. Journal of Structural Geology 6, 449–458.

Schreurs, G., Colletta, B., 1998. Analogue modelling of faulting in zones of continental transpression and transtension. In: Holdsworth, R.E., Strachan, R.A., Dewey, J.F. (Eds.), Continental Transpressional and Transtensional Tectonics. Geological Society of London Special Publication, vol. 135, pp. 59–79.

Segall, P., Pollard, D.D., 1980. Mechanics of discontinuous faults. Journal of Geophysical Research 85, 4337–4350.
Sornette, A., Davy, P., Sornette, D., 1993. Fault growth in brittle-ductile experiments and the mechanics of continental collisions. Journal of Geophysical Research 98, 12111–12139.
Storti, F., Holdsworth, R.E., Salvini, F., 2003. Intraplate strike-slip deformation belts. In: Storti, F., Holdsworth, R.E., Salvini, F. (Eds.), Intraplate Strike-slip Deformation Belts. Geological Society of London Special Publication, vol. 210, pp. 1–14.
Sylvester, A.G., 1988. Strike-slip faults. Geological Society of America Bulletin 100, 1660–1703.
Tchalenko, J.S., 1968. The evolution of kink-bands and the development of compression textures in sheared clays. Tectonophysics 6, 159–174.
Tchalenko, J.S., 1970. Similarities between shear zones of different magnitudes. Geological Society of America Bulletin 81, 1625–1640.
Ueta, K., Tani, K., Kato, T., 2000. Computerized X-ray tomography analysis of three dimensional fault geometries in basement-induced wrench faulting. Engineering Geology 56, 197–210.
Viola, G., Mancktelow, N.S., Seward, D., 2001. Late Oligocene-Neogene evolution of Europe-Adria collision: new structural and geochronological evidence from the Giudicarie fault system (Italian eastern Alps). Tectonics 20, 999–1020.
Viola, G., Odonne, F., Mancktelow, N.S., 2004. Analogue modelling of reverse fault reactivation in strike-slip and transpressive regimes: application to the Giudicarie fault system, Italian Eastern Alps. Journal of Structural Geology 36, 401–418.
Weijermars, R., Schmeling, H., 1986. Scaling of Newtonian and non-Newtonian fluid dynamics without inertia for quantitative modelling of rock flow due to gravity (including the concept of rheological similitary). Physics of the Earth and Planetary Interiors 43, 316–330.
Wilcox, R.E., Harding, T.P., Seely, D.R., 1973. Basic wrench fault tectonics. American Association of Petroleum Geologists Bulletin 57, 74–96.